NANO LETTERS

pubs.acs.org/NanoLett Letter

Silicon Nanomembrane-Based Synaptic Photodetectors Activated by Phosphorescent Stacks

Xiaozhong Wu, Haonan Zhao, Zhongying Xue, Yongfeng Mei, Zengfeng Di,* and Qinglei Guo*

Cite This: *Nano Lett.* 2025, 25, 11836−11843 Read Online

ACCESS | Metrics & More | Article Recommendations | Supporting Information

ABSTRACT: Neuromorphic computing that mimics the human brain to realize efficient parallel information processing is considered an important path to break the von Neumann bottleneck. Optoelectronic synaptic devices are of particular interest because of their critical role in the development of neuromorphic computing. This work presents a synaptic photodetector based on the hybrid structure from silicon nanomembranes and a phosphorescent film. The bright and lasting green afterglow of phosphorescent film can be absorbed by the underneath silicon nanomembranes, thus leading to persistent photoconduction. Consequently, synaptic functionalities including excitatory postsynaptic current (EPSC) and paired-pulse facilitation (PPF) are realized via the optical stimulations. Moreover, synaptic short-term and long-term plasticity can be selectively defined within the devices, which are further utilized to simulate age-related cognitive states and memory processes. These results add to the portfolio of optoelectronic synapse options in neuromorphic computing, artificial intelligence, and visual perception systems.

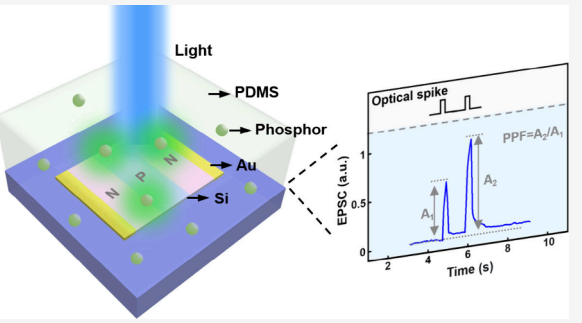

KEYWORDS: *optoelectronic synaptic device, silicon nanomembrane, photodetector, neuromorphic vision, synaptic plasticity*

Recently, neuromorphic engineering has emerged as a transformative paradigm for developing artificial systems that emulate the computational efficiency and adaptive learning capabilities of biological neural networks.[1−4] Among biological inspirations, the human visual system stands out as a critical research focus because approximately 80% of external sensory information to humans is received through vision.[5,6] This biological blueprint has driven the development of neuromorphic vision systems, which demonstrate remarkable potentials in artificial intelligence,[7−10] in-sensor computing,[11−15] and image recognition.[16−19] Central to these achievements are optoelectronic synaptic devices that bridge optoelectronic sensing with neuromorphic computing to mimic the behavior of biological visual synapses.[20−25] Consequently, various functional materials, such as metal oxides,[26,27] perovskites,[28,29] two-dimensional layered materials,[30,31] and silicon,[32,33] have been employed to fabricate optoelectronic synaptic devices. For the sake of large-area fabrication of high-performance optoelectronic synaptic devices, the silicon nanomembrane has emerged as a promising candidate owing to its natural compatibility with the state-of-the-art semiconductor technology.[34−37]

To enable the synaptic behavior of silicon nanomembrane-based optoelectronic devices, surface modifications or hybrid structure integrations to manipulate the transport of photogenerated carriers are required. For example, rough silicon nanomembranes that have abundant dangling bonds at the surface can trap and release photogenerated carriers, thus enabling persistent photoconduction after the illuminated light is removed.[38,39] The hybrid integration of silicon nanomembranes with carrier transport layers, such as perovskite[34] and poly(3-hexylthiophene),[40] leads to a distinct photogating effect, which builds up the fundamentals for synaptic functionalities existing in silicon nanomembrane-based phototransistors. Despite the remarkable achievements, most of the demonstrated devices rely on manipulating the triggering signal to modulate the synaptic plasticity,[41−43] i.e., small input for short-term plasticity (STP) and high or repeated input for long-term plasticity (LTP). Therefore, repetitively training artificial neural networks with numerous data sets is required to take advantage of both STP and LTP.[1] In addition, currently available silicon nanomembrane-based optoelectronic synaptic devices also involve one or more disadvantages in complex fabrication, susceptible material properties, and/or obscure working principle.

In this work, we propose an approach for the convenient fabrication of a silicon nanomembrane-based synaptic photodetector that consists of an upper phosphorescent film and a

Received: April 11, 2025
Revised: July 24, 2025
Accepted: July 24, 2025
Published: July 28, 2025

https://doi.org/10.1021/acs.nanolett.5c02135
Nano Lett. 2025, 25, 11836−11843

lower silicon nanomembrane-based photodetector. The afterglow of $SrAl_2O_4:Eu^{2+},Dy^{3+}$ phosphors doped in the phosphorescent film leads to persistent photoconduction of the underneath silicon nanomembranes, which fundamentally enables the synaptic functionalities, including excitatory postsynaptic current (EPSC) and paired-pulse facilitation (PPF). Moreover, through controlling the doping concentration of the $SrAl_2O_4:Eu^{2+},Dy^{3+}$ phosphor in phosphorescent films, synaptic plasticity, i.e., STP and LTP, can be straightforwardly and selectively defined in silicon nanomembrane-based photodetectors. Furthermore, age-related cognitive states and memory processes are successfully simulated by manipulating the plasticity of a synaptic photodetector array. We expect that the demonstrated silicon nanomembrane-based synaptic photodetector will provide an accurate and versatile platform for the application of artificial intelligence, image recognition, and visual perception systems.

Figure 1a shows a schematic of the human visual system as well as a typical biological synapse that implements the neural signal transmission. Light perceived by the photoreceptors in the retina will be converted into a neural stimulus, which triggers the release of neurotransmitters. These neurotransmitters are eventually received by the postsynaptic neuron, thus enabling a variety of visual perceptions. To simulate the neuromorphic vision system, an optoelectronic synaptic photodetector is developed. As shown in Figure 1b, the synaptic photodetector has a hybrid structure in which a phosphorescent film stacks on top of a silicon-based photodetector. The phosphorescent film is composed of $SrAl_2O_4:Eu^{2+},Dy^{3+}$ phosphors and polydimethylsiloxane (PDMS). Notably, $SrAl_2O_4:Eu^{2+},Dy^{3+}$, known as one of the longest afterglow phosphors with high brightness,[44] determines the synaptic behavior of the proposed synaptic photodetector. The detailed phosphorescence mechanism of $SrAl_2O_4:Eu^{2+},Dy^{3+}$ can be found in Figure S1, and the corresponding descriptions in the Supporting Information. As schematically illustrated in Figure 1c, the $SrAl_2O_4:Eu^{2+},Dy^{3+}$/PDMS phosphorescent film could emit a bright and lasting green afterglow after turning-off the excited light. As a result, the emitted afterglow can be absorbed by the underneath silicon nanomembrane, thus leading to a persistent photoconduction of the corresponding silicon-based photodetector, as displayed in the top panel of Figure 1d. With a pair of light excitation spikes, typical PPF occurs, as schematically shown in the bottom panel of Figure 1d, which is similar to the behavior of biological synapses. Moreover, selectively definable synaptic plasticity, including LTP and STP, could be achieved by controlling the weight ratio of the $SrAl_2O_4:Eu^{2+},Dy^{3+}$ phosphor to PDMS, as presented in Figure 1e.

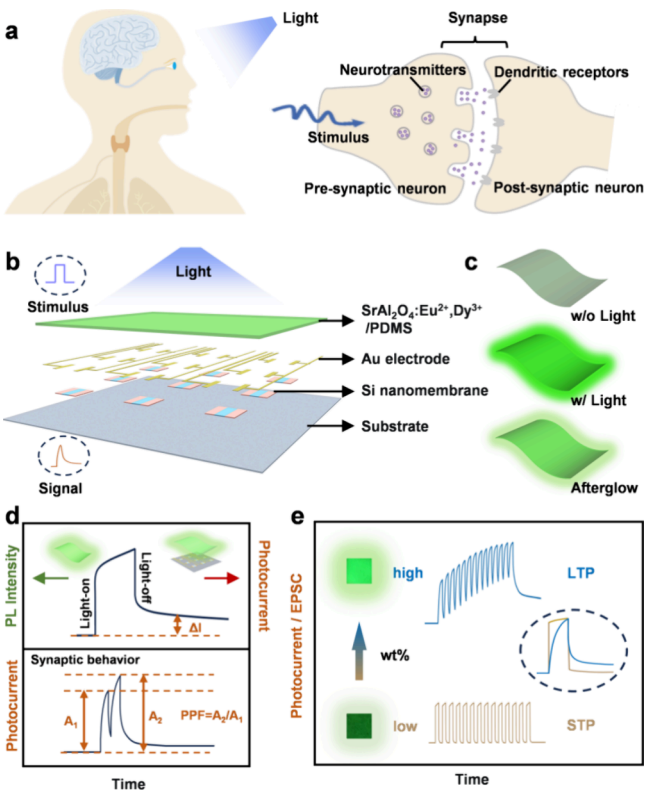

Figure 1. (a) Schematic of the human visual system and the neural signal transmission in a biological synapse. (b) Exploded diagram of key materials and components of the synaptic photodetector. (c) Schematics of the phosphorescent film at different states. A bright and green afterglow can be emitted after the light excitation. (d) Conceptual illustrations of the phosphorescence of phosphorescent films excited with an optical spike, and the induced photocurrent of synaptic photodetectors. Triggered with a pair of optical spikes, typical paired pulse facilitation (PPF) behavior can be observed. (e) Schematic of excitatory postsynaptic current (EPSC) for long-term plasticity (LTP, top) and short-term plasticity (STP, bottom) synaptic photodetectors.

The scanning electron microscopy (SEM) image of the utilized $SrAl_2O_4:Eu^{2+},Dy^{3+}$ phosphor is shown in Figure 2a, and the average particle size is 18 μm (Figure S2). Figure 2b shows the X-ray diffraction (XRD) pattern of the phosphor, which agrees well with the standard pattern of $SrAl_2O_4:Eu^{2+},Dy^{3+}$. The absorption spectrum in Figure 2c indicates that the $SrAl_2O_4:Eu^{2+},Dy^{3+}$ phosphor can be effectively excited by light with a wavelength range of 360−430 nm. Therefore, in the following optoelectronic characterizations on the synaptic photodetector, a 405 nm laser is used as the excitation light. Besides, the corresponding emission spectrum reveals a peak position around 520 nm, well-located within the effective photodetection range of silicon-based photodetectors.[45] The phosphorescence property of $SrAl_2O_4:Eu^{2+},Dy^{3+}$ is measured by a fluorescence spectrophotometer. As shown in Figure 2d, the phosphorescence intensity gradually increases with the continuous excitation of light and eventually saturates. After stopping the light excitation, the phosphorescence intensity undergoes a rapid decay, followed by a gradual decay with obvious afterglow.

For the convenient integration with silicon-based photodetectors, $SrAl_2O_4:Eu^{2+},Dy^{3+}$ phosphor powder is dispersed into PDMS precursor, as the resulting aqueous composite can be spin-coated onto a planar substrate (Figure S3). After being fully cured, phosphorescent films, with tunable thickness with the spin-coating speed (Figure S4), can be obtained. $SrAl_2O_4:Eu^{2+},Dy^{3+}$ phosphor particles are uniformly distributed in the phosphorescent film, as verified by the energy dispersive spectroscopy (EDS) mapping results in Figure S5, thus providing homogeneous emission of the afterglow. Figure 2e shows the phosphorescence properties of $SrAl_2O_4:Eu^{2+},Dy^{3+}$/PDMS phosphorescent films with different weight ratios. Obviously, the higher weight ratio of $SrAl_2O_4:Eu^{2+},Dy^{3+}$ to PDMS leads to a much stronger phosphorescence intensity in either the excitation or afterglow period. Figure 2f shows optical images of the phosphorescent film before and after the light excitation. Due to the phosphorescent property of

https://doi.org/10.1021/acs.nanolett.5c02135
Nano Lett. 2025, 25, 11836−11843

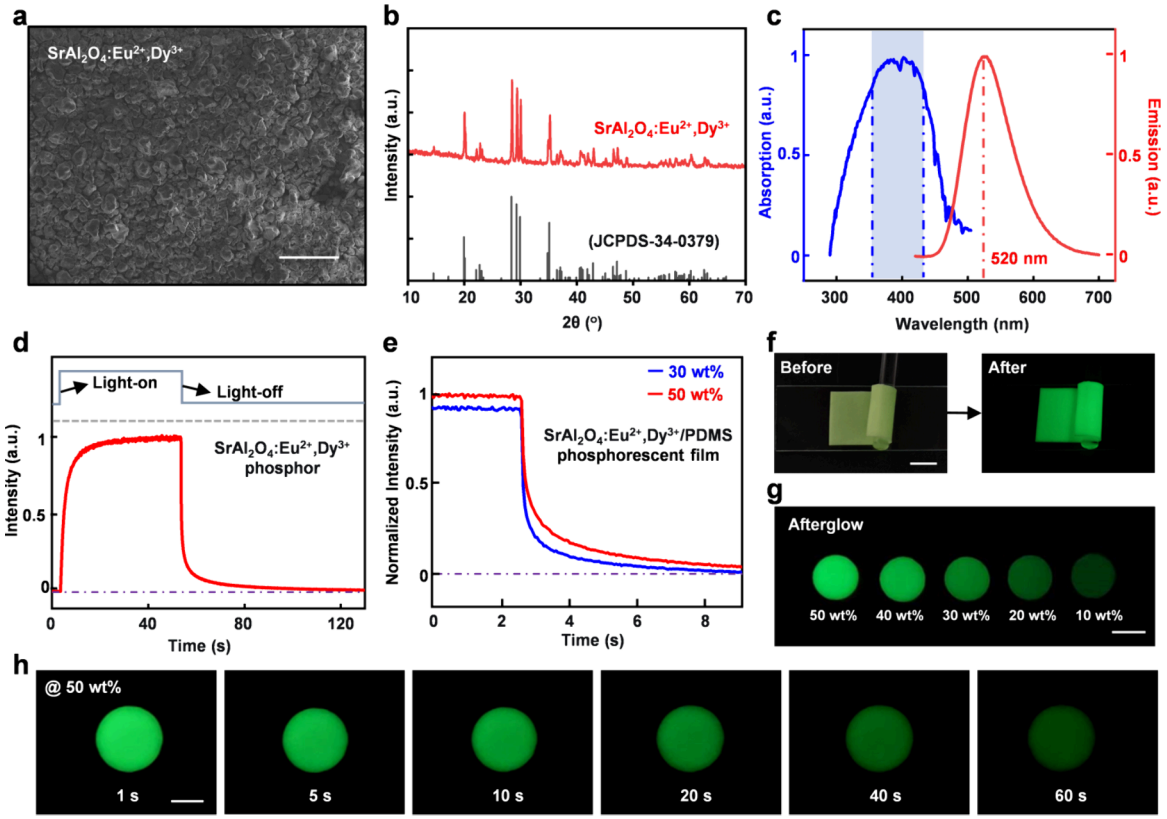

Figure 2. Characterizations on the $SrAl_2O_4:Eu^{2+},Dy^{3+}$ phosphor: (a) SEM image, scale bar: 100 μm. (b) XRD pattern. (c) Absorption and emission spectra (excitation wavelength: 400 nm). (d) Phosphorescent lifetime. (e) Normalized phosphorescent intensity of $SrAl_2O_4:Eu^{2+},Dy^{3+}$/PDMS phosphorescent film with different weight ratios varying with the time. (f) Optical images of phosphorescent film before and after illumination (scale bar: 1 cm). (g) Optical images of phosphorescent films with different weight ratios after the same light illumination (scale bar: 1 cm). (h) Optical images of the phosphorescence decay of 50 wt % phosphorescent film (scale bar: 0.5 cm).

$SrAl_2O_4:Eu^{2+},Dy^{3+}$, the phosphorescent film after illumination emits a bright and green afterglow, of which the corresponding intensity is strongly related to the weight ratio of $SrAl_2O_4:Eu^{2+},Dy^{3+}$ to PDMS, as evidenced in Figure 2g. For the phosphorescent film with a weight ratio of 50%, persistent afterglow emission is observed, as revealed in Figure 2h. Notably, these optical images could only provide a qualitative exhibition of the afterglow, since the image quality is strongly related to detailed settings of the used digital camera. These presented results lay down the foundations to manipulate the synaptic behaviors of the proposed synaptic photodetector.

Another key component of the proposed synaptic device is a silicon-based photodetector that captures the emitted afterglow of the upper phosphorescent film, then performs as an optoelectronic synaptic device. In other words, a silicon-based photodetector serves as the "bridge" to connect two seemingly irrelevant phenomena, i.e., phosphorescent behavior and synaptic behavior. In this regard, silicon nanomembrane-based photodetectors, with a typical NPN structure (Figure S6),[35,46] are fabricated by utilizing silicon-on-insulator (SOI), as shown in Figure 3a. Figure 3b shows the current−voltage characteristics of the photodetector under various light illumination conditions. Due to the photoconduction effect, significant enhancement in the current can be observed. Moreover, the photodetector can rapidly track the optical spike (wavelength: 405 nm, power density: 1.53 mW/mm^2, duration: 1.5 s), with steep light-on and light-off edges, as revealed in Figure 3c. By utilizing the transfer printing technique (Figure S7), flexible photodetectors with good mechanical robustness are available (Figure S8), thus offering potential for the fabrication of flexible synaptic devices. After integrating with $SrAl_2O_4:Eu^{2+},Dy^{3+}$/PDMS phosphorescent film, the resulting synaptic photodetector (Figure S9) could exhibit typical EPSC. Besides, the EPSC can be modulated by the doping concentration of $SrAl_2O_4:Eu^{2+},Dy^{3+}$ in the integrated phosphorescent film. As shown in Figure 3d, high doping concentration, e.g., 50 wt %, causes large EPSC during the decay period, which is similar to the phosphorescent characteristics of phosphorescent films (see Figure 2e). This doping concentration-dependent EPSC decay provides convenience to deterministically define the plasticity, i.e., LTP and STP, of the synaptic photodetectors.

Triggered by a pair of optical spikes with a duration (t) of 0.2 s and an interval (Δt) of 1 s, typical PPF behavior can be simulated by the synaptic photodetector, as shown in Figure 3e. Moreover, the PPF index is strongly related to the weight ratio of $SrAl_2O_4:Eu^{2+},Dy^{3+}$ to PDMS in phosphorescent films. As summarized in Figure 3f, within the low weight ratio range of $SrAl_2O_4:Eu^{2+},Dy^{3+}$ (10−30%), the excited light that penetrates the phosphorescent film dominates the optoelectronic responses of the synaptic photodetector. Consequently, PPF undergoes a moderate increase. As the weight ratio increases (30−50%), both the phosphorescence emitted from doped phosphors and excited light could contribute to the optoelectronic responses. Introducing more doped phosphors could significantly strengthen the synaptic behavior. As a result, PPF exhibits a rapid increase. At the high weight ratio range (50−70%), the phosphorescence emitted from doped

https://doi.org/10.1021/acs.nanolett.5c02135
Nano Lett. 2025, 25, 11836−11843

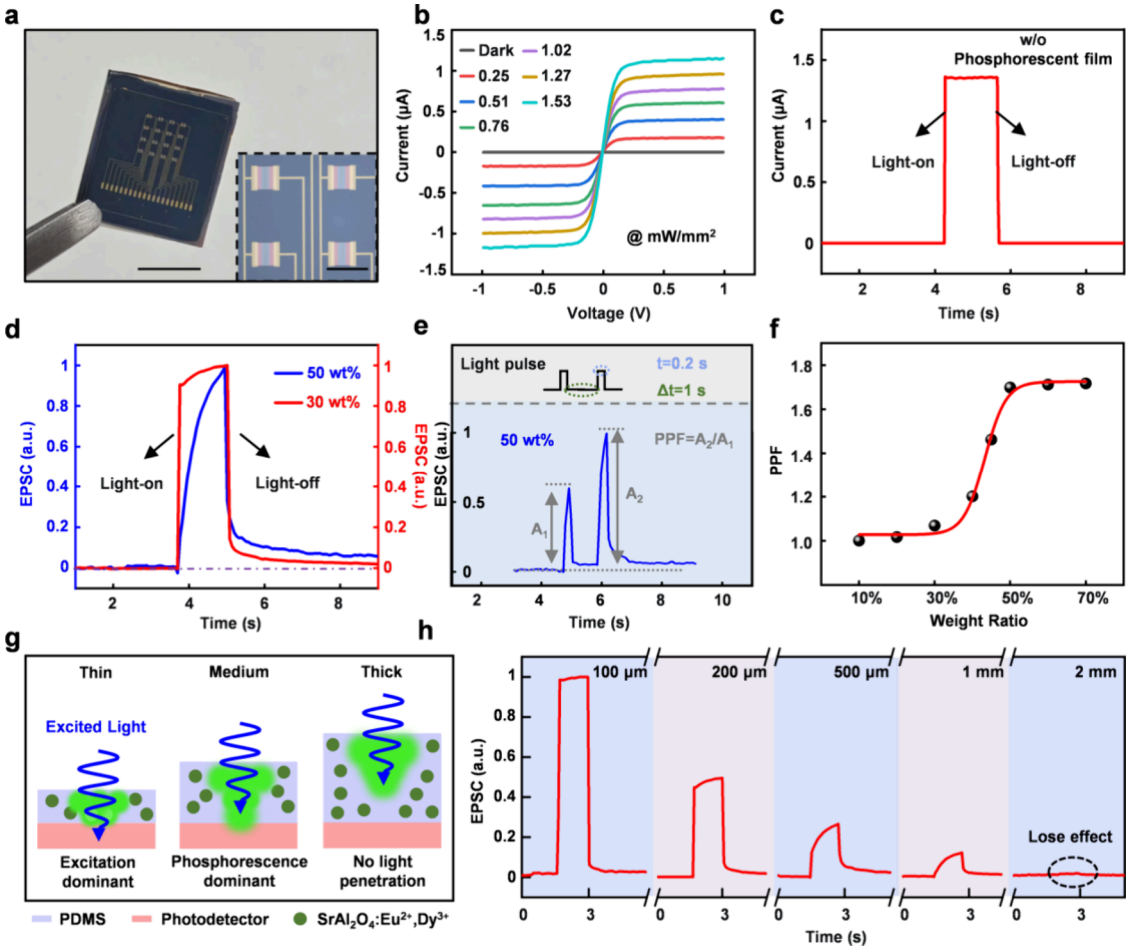

Figure 3. (a) Optical images of a silicon-based NPN photodetector array (scale bar: 0.5 cm). The inset shows the optical microscope image (scale bar: 500 μm). (b) Current−voltage characteristics of the photodetector under various light illumination conditions (laser wavelength: 405 nm). (c) Photocurrents varying with a pulsed laser. (d) EPSC of synaptic photodetectors with different weight ratios of $SrAl_2O_4:Eu^{2+},Dy^{3+}$ in phosphorescent films. (e) PPF behavior of the synaptic photodetector by a pair of optical spikes. (f) PPF index as a function of the doping concentration of integrated phosphorescent films for synaptic photodetectors. (g) Schematics of the light penetration and phosphorescence distribution in phosphorescent films with different thicknesses. (h) EPSC of synaptic photodetectors with different thicknesses of phosphorescent films under a light pulse.

phosphors will dominate the optoelectronic responses. As the weight ratio continues to increase, the synaptic behavior of the photodetector is similar to the intrinsic phosphorescent property of phosphors, thus inducing a gradual saturation of the PPF. Therefore, the weight ratio is optimized as 50%, with which the synaptic photodetector can achieve a high PPF (1.62) that is comparable with or higher than previously reported values though the triggering condition varies, as summarized in Table S1. More details about the EPSC of different synaptic photodetectors triggered with the same pair of optical spikes can be found in Figure S10.

Additionally, the thickness of the phosphorescent film is another important factor that affects the performance of synaptic photodetectors. Figure 3g illustrates the model to describe the light penetration and phosphorescence distribution within phosphorescent films with different thicknesses but the same doping concentration of $SrAl_2O_4:Eu^{2+},Dy^{3+}$. For the thin phosphorescent film with weak phosphorescence intensity, the excited light can readily penetrate it to enter the photodetector, dominating the optoelectronic response of the synaptic photodetector. On the other hand, a too-thick phosphorescent film will prevent both the excited light and phosphorescence from penetrating the film to reach the photodetector, thus inducing a negligible optoelectronic response. For the phosphorescent film with optimal thickness, phosphorescence will dominate the optoelectronic response particularly during the light-off period. These analyses are corroborated by the EPSC characteristics of synaptic photodetectors with varying phosphorescent film thicknesses, as demonstrated in Figure 3h. Accordingly, the phosphorescent film thickness is ultimately optimized as 500 μm.

For the synaptic photodetector with optimal thickness, as well as the doping concentration of $SrAl_2O_4:Eu^{2+},Dy^{3+}$, of the phosphorescent film, the EPSC can be also modulated by the light triggering condition. As shown in Figure 4a, the time interval (Δt) between two optical spikes strongly affects the EPSC. The calculated PPF index exponentially decays as Δt increases, as evidenced in Figure 4b. More details about the EPSC measured with varying time intervals can be found in Figure S11. At identical optical spike intervals (Δt), the PPF magnitude also exhibits an inverse correlation with optical spike duration (t) (see Figure S12). Figure 4c depicts the EPSC triggered with 2 and 14 optical spikes. The optical spike mimics the learning activity for a person. Particularly, the

https://doi.org/10.1021/acs.nanolett.5c02135
Nano Lett. 2025, 25, 11836−11843

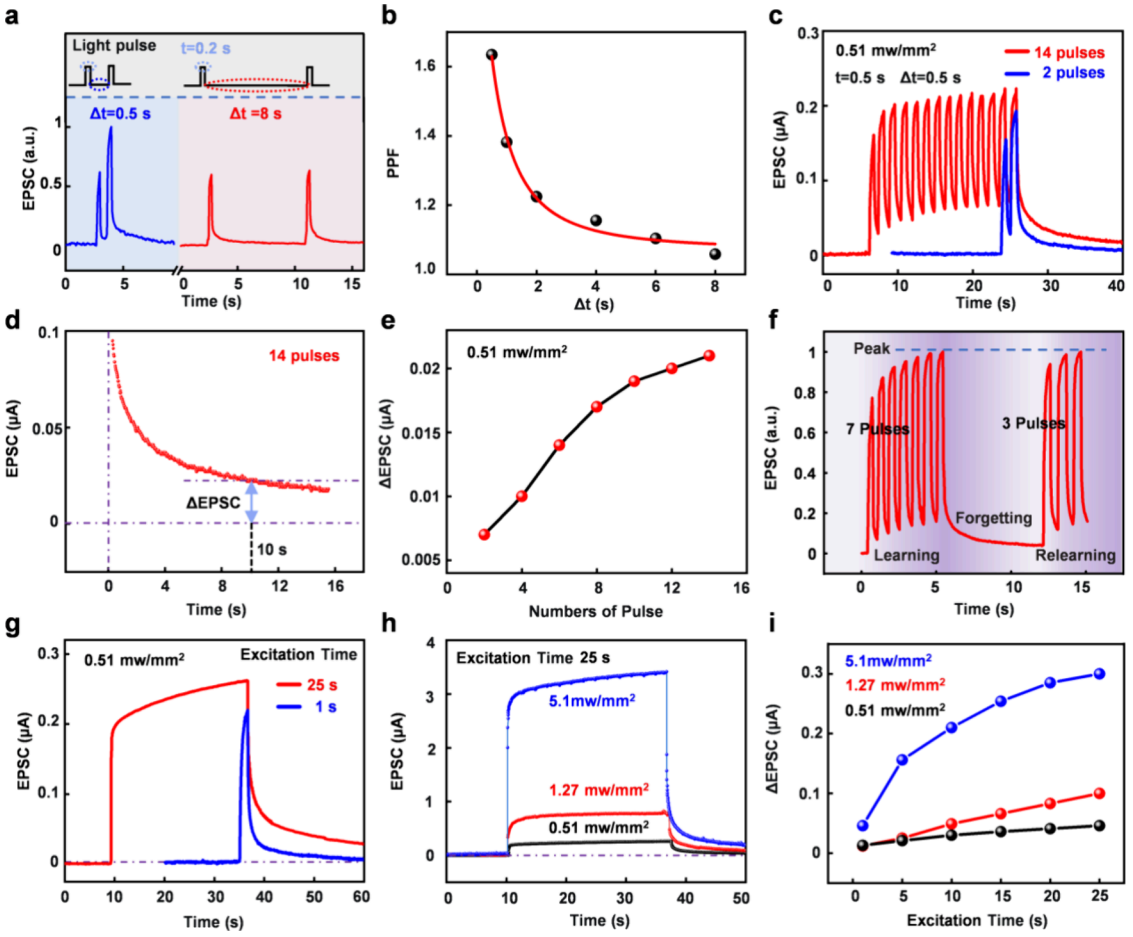

Figure 4. Characterizations on the synaptic photodetector. (a) PPF triggered by optical spike pairs with two typical interval times. (b) PPF index as a function of optical spike interval time. (c) EPSC triggered by 2 and 14 optical spikes, and both duration and interval time are 0.5 s. (d) EPSC decay triggered by 14 optical spikes, and ΔEPSC is the difference between the EPSC following cessation of illumination for 10 s and the initial EPSC. (e) ΔEPSC varying with the number of triggered optical spikes. (f) "Learning−forgetting−relearning" training triggered by multiple optical spikes. (g) EPSC triggered by optical spikes with two different durations. (h) EPSC triggered by optical spikes with three different light power densities. (i) ΔEPSC as a function of the duration for three different light power densities.

difference between the EPSC following cessation of illumination for 10 s and the initial EPSC is defined as ΔEPSC (Figure 4d), which is utilized to emulate the memory strength. Obviously, more repetitions of learning activities facilitate strengthening the memory, as revealed in Figure 4e. Moreover, the human cognitive process of "learning−forgetting−relearning" is emulated by the synaptic photodetector. As shown in Figure 4f, the initial learning with 7 optical spikes significantly enhances the EPSC, followed by a gradual decrease during a 7 s forgetting process. Nevertheless, a relearning process employed with only 3 optical spikes could reach the same potentiation as the initial learning. In addition, the memory strength is also related to both the duration (Figure 4g) and intensity (Figure 4h) of the triggered optical spike. As demonstrated in Figure 4i and Figure S13, either a longer duration or a larger illumination intensity leads to a much stronger ΔEPSC. These characteristics of the proposed synaptic photodetector are highly similar to the visual memory behavior of the human.

To simulate the human visual memory behavior, a 3 × 3 array of synaptic photodetectors is fabricated for image recognition and memorization. As illustrated in Figure 5a, the light source passes through a mask with the letter "T" to selectively illuminate the device array. Figure 5b shows the EPSC of a typical synaptic photodetector, which is triggered with an optical spike (duration: 25 s; power density: 5.1 mW/mm^2). The EPSC at three specific moments following termination of illumination, as highlighted in Figure 5b with blue circles, is utilized to visualize the forgetting process. For human visual memory, the corresponding capability is strongly related to the learning ability and learning time, which can be emulated by the plasticity and optical spike duration of the synaptic photodetector, respectively, as illustrated in Figure S14. In particular, the age-related learning ability decline can be simulated by manipulating the plasticity (LTP or STP) of the synaptic photodetector, which is conveniently attainable by controlling the weight ratio of doped phosphor in the integrated phosphorescent films. As depicted in Figure 5c, for the LTP device array (weight ratio: 50 wt %), a prolonged optical spike duration (corresponds to learning time) leads to clearer memory. With the same learning time (25 s), the STP device array (weight ratio: 30 wt %), however, exhibits declined memory capability. These presented results suggest the potential of the proposed synaptic photodetectors to simulate authentic biological activities.

For potential applications in the artificial visual system, two main challenges may exist in the present design of synaptic photodetectors, i.e., i) locally integrating the phosphorescent

https://doi.org/10.1021/acs.nanolett.5c02135
Nano Lett. 2025, 25, 11836−11843

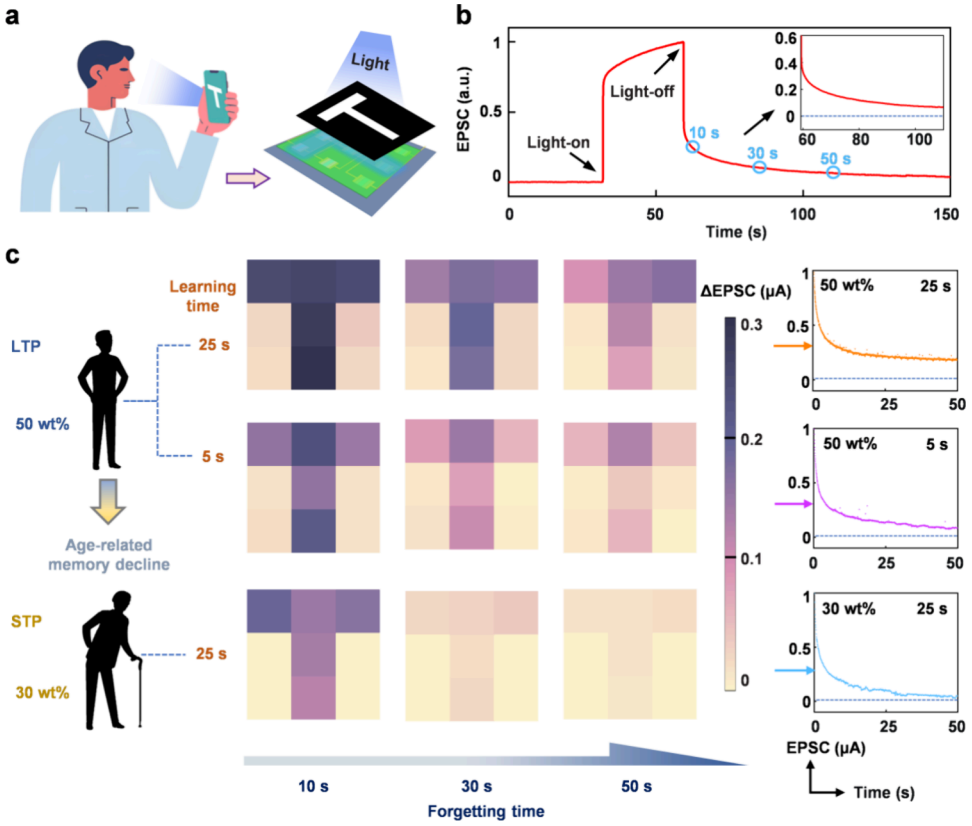

Figure 5. (a) Schematic of human visual system and synaptic photodetector array. (b) The EPSC of the synaptic photodetector triggered with an optical spike; three specific moments following termination of illumination are highlighted to visualize the forgetting process. (c) ΔEPSC changes of the synaptic photodetector array under different conditions to illustrate the learning time related memory loss (top and middle panels) and the age-related memory loss (top and bottom panels). EPSC decay of a typical synaptic photodetector corresponding to the three conditions is shown on the right.

films on the photodetector pixel to form the compact device; ii) multispectral photodetection. For the former one, the phosphorescent film array can be well aligned and locally integrated with the underlying photodetection pixel array to form a functional and compact flexible synaptic photodetector array, as shown in Figure S15 with the relevant descriptions in the Supporting Information. In addition, the flexible synaptic photodetector with locally integrated phosphorescent film exhibits better mechanical robustness in comparison to the device with a large-area phosphorescent film, as shown in Figure S16 with the corresponding descriptions in the Supporting Information. For the latter one, a synaptic photodetector with multispectral photodetection, in our opinion, could be well suited for an artificial visual system. The fabricated $SrAl_2O_4:Eu^{2+},Dy^{3+}$-based synaptic photodetector has an excitation band of 360−430 nm. Integrating such a device with another two or more synaptic photodetectors, which respectively have a narrow but different wavelength band for effective triggering, will provide new possibilities for mimicking the artificial visual system. For this purpose, the $Sr_{0.75}Ca_{0.25}S:Eu^{2+}$ phosphor,[15,47] with an excitation band of 420−540 nm, has been utilized to fabricate synaptic photodetectors (see the detailed results in Figures S17−S19 and discussions in the Supporting Information). Despite suitable phosphorescent materials that have a narrow wavelength band close to red light and long afterglow being presently scarce, the rapid development of materials science is expected to facilitate the multispectral photodetection required for artificial visual systems.

In summary, we have demonstrated synaptic photodetectors based on the hybrid integration of silicon nanomembranes and phosphorescent films. Owing to the afterglow characteristics of the stacked phosphorescent films, synaptic functionalities, including EPCS and PPF, can be conveniently activated within silicon nanomembrane-based photodetectors. Under different light illumination conditions, including varying light pulse intervals, pulse numbers, and power densities, human visual memory and cognitive behaviors are successfully simulated by the fabricated synaptic photodetectors. Moreover, selectively defined synaptic plasticity, including STP and LTP, is available by controlling the weight ratio of the phosphor in the phosphorescent film. As a proof of concept, two 3 × 3 arrays of synaptic photodetectors with distinct plasticity are fabricated and age-related learning ability and memory decline are successfully simulated. These presented results suggest great potentials of the demonstrated silicon nanomembrane-based synaptic photodetector to serve as an accurate and versatile platform for applications in artificial intelligence, image recognition, and visual perception systems.

■ ASSOCIATED CONTENT

Data Availability Statement

The data that support the findings of this study are available from the corresponding author upon reasonable request.

https://doi.org/10.1021/acs.nanolett.5c02135
Nano Lett. 2025, 25, 11836−11843

Supporting Information

The Supporting Information is available free of charge at https://pubs.acs.org/doi/10.1021/acs.nanolett.5c02135.

Detailed experimental methods for device fabrication and characterizations; corresponding interpretations for phosphorescence mechanism, mechanical characterizations of flexible synaptic photodetectors, and $Sr_{0.75}Ca_{0.25}S:Eu^{2+}$-based synaptic photodetectors; additional results with dedicated captions describing the context (PDF)

AUTHOR INFORMATION

Corresponding Authors

Zengfeng Di − *State Key Laboratory of Materials for Integrated Circuits, Shanghai Institute of Microsystem and Information Technology, Chinese Academy of Sciences, Shanghai 200050, P. R. China;* orcid.org/0000-0002-9357-5107; Email: zfdi@mail.sim.ac.cn

Qinglei Guo − *School of Integrated Circuits, Shandong University, Jinan 250100, P. R. China; State Key Laboratory of Materials for Integrated Circuits, Shanghai Institute of Microsystem and Information Technology, Chinese Academy of Sciences, Shanghai 200050, P. R. China;* orcid.org/0000-0002-6319-037X; Email: qlguo@sdu.edu.cn

Authors

Xiaozhong Wu − *School of Integrated Circuits, Shandong University, Jinan 250100, P. R. China*

Haonan Zhao − *School of Integrated Circuits, Shandong University, Jinan 250100, P. R. China*

Zhongying Xue − *State Key Laboratory of Materials for Integrated Circuits, Shanghai Institute of Microsystem and Information Technology, Chinese Academy of Sciences, Shanghai 200050, P. R. China*

Yongfeng Mei − *Department of Materials Science, International Institute for Intelligent Nanorobots and Nanosystems, Fudan University, Shanghai 200438, P. R. China;* orcid.org/0000-0002-3314-6108

Complete contact information is available at: https://pubs.acs.org/10.1021/acs.nanolett.5c02135

Notes

The authors declare no competing financial interest.

ACKNOWLEDGMENTS

This work was supported by National Key R&D Program of China (Grant No. 2022YFB3204800), the STI 2030-Major Projects (Grant No. 2022ZD0209900), the National Natural Science Foundation of China (Grant No. 62375054), Science and Technology Commission of Shanghai Municipality (Grant Nos. 24520750200 and 24CL2900200), Shanghai Talent Programs, CAS Project for Young Scientists in Basic Research (Grant No. YSBR-081), Strategic Priority Research Program of the Chinese Academy of Sciences (Grant No. XDB0670000), and the Open Research Fund of State Key Laboratory of Materials for Integrated Circuits (Grant No. SKLJC-K2024-02).

REFERENCES

(1) Choi, Y.; Ho, D.; Kim, S.; Choi, Y.; Roe, D.; Kwak, I.; Min, J.; Han, H.; Gao, W.; Cho, J. Physically defined long-term and short-term synapses for the development of reconfigurable analog-type operators capable of performing health care tasks. *Sci. Adv.* **2023**, *9*, No. eadg5946.

(2) Liu, J.; Jiang, C.; Wei, H.; Wang, Z.; Sun, L.; Zhang, S.; Ni, Y.; Qu, S.; Yang, L.; Xu, W. Vertically integrated monolithic neuromorphic nanowire device for physiological information processing. *Nano Lett.* **2024**, *24*, 4336−4345.

(3) Wang, W.; Wang, Y.; Yin, F.; Niu, H.; Shin, Y.-K.; Li, Y.; Kim, E.-S.; Kim, N.-Y. Tailoring classical conditioning behavior in TiO_2 nanowires: ZnO QDs-based optoelectronic memristors for neuromorphic hardware. *Nano-Micro Lett.* **2024**, *16*, 133.

(4) Qu, S.; Sun, L.; Zhang, S.; Liu, J.; Li, Y.; Liu, J.; Xu, W. An artificially-intelligent cornea with tactile sensation enables sensory expansion and interaction. *Nat. Commun.* **2023**, *14*, 7181.

(5) Chen, L.; Li, R.; Yuan, S.; Chen, A.; Li, Y.; Zhang, T.; Wei, L.; Zhang, Q.; Li, Q. Fiber-shaped artificial optoelectronic synapses for wearable visual-memory systems. *Matter* **2023**, *6*, 925−939.

(6) Gu, L.; Poddar, S.; Lin, Y.; Long, Z.; Zhang, D.; Zhang, Q.; Shu, L.; Qiu, X.; Kam, M.; Javey, A.; Fan, Z. A biomimetic eye with a hemispherical perovskite nanowire array retina. *Nature* **2020**, *581*, 278−282.

(7) Fang, H.; Ma, S.; Wang, J.; Zhao, L.; Nie, F.; Ma, X.; Lü, W.; Yan, S.; Zheng, L. Multimodal in-sensor computing implemented by easily-fabricated oxide-heterojunction optoelectronic synapses. *Adv. Funct. Mater.* **2024**, *34*, 2409045.

(8) Liu, X.; Wang, D.; Chen, W.; Kang, Y.; Fang, S.; Luo, Y.; Luo, D.; Yu, H.; Zhang, H.; Liang, K.; Fu, L.; Ooi, B. S.; Liu, S.; Sun, H. Optoelectronic synapses with chemical-electric behaviors in gallium nitride semiconductors for biorealistic neuromorphic functionality. *Nat. Commun.* **2024**, *15*, 7671.

(9) Liu, Y.; Liu, D.; Gao, C.; Zhang, X.; Yu, R.; Wang, X.; Li, E.; Hu, Y.; Guo, T.; Chen, H. Self-powered high-sensitivity all-in-one vertical tribo-transistor device for multi-sensing-memory-computing. *Nat. Commun.* **2022**, *13*, 7917.

(10) Wang, Y.; Zhang, Z.; Xu, M.; Yang, Y.; Ma, M.; Li, H.; Pei, J.; Shi, L. Self-doping memristors with equivalently synaptic ion dynamics for neuromorphic computing. *ACS Appl. Mater. Interfaces* **2019**, *11*, 24230−24240.

(11) Zhang, Y.; Wang, B.; Han, Z.; Shi, X.; Zhang, N.; Miao, T.; Lin, D.; Jiang, Z.; Liu, M.; Guo, H.; Zhang, J.; Hu, H.; Wang, L. Bidirectional photoresponse in a mixed-dimensional MoS_2/Ge heterostructure and its optic-neural synaptic behavior for colored pattern recognition. *ACS Photonics* **2023**, *10*, 1575−1582.

(12) Sheng, X.; Yu, C.; Malyarchuk, V.; Lee, Y. H.; Kim, S.; Kim, T.; Shen, L.; Horng, C.; Lutz, J.; Giebink, N. C.; Park, J.; Rogers, J. A. Silicon-based visible-blind ultraviolet detection and imaging using down-shifting luminophores. *Adv. Opt. Mater.* **2014**, *2*, 314−319.

(13) Baek, E.; Song, S.; Baek, C.-K.; Rong, Z.; Shi, L.; Cannistraci, C. V. Neuromorphic dendritic network computation with silent synapses for visual motion perception. *Nat. Electron.* **2024**, *7*, 454−465.

(14) Mukherjee, S.; Dutta, D.; Ghosh, A.; Koren, E. Graphene-In_2Se_3 van der Waals heterojunction neuristor for optical in-memory bimodal operation. *ACS Nano* **2023**, *17*, 22287−22298.

(15) Guo, J.; Guo, F.; Zhao, H.; Yang, H.; Du, X.; Fan, F.; Liu, W.; Zhang, Y.; Tu, D.; Hao, J. In-sensor computing with visual-tactile perception enabled by mechano-optical artificial synapse. *Adv. Mater.* **2025**, *37*, No. 2419405.

(16) Wang, X.; Yang, S.; Qin, Z.; Hu, B.; Bu, L.; Lu, G. Enhanced multiwavelength response of flexible synaptic transistors for human sunburned skin simulation and neuromorphic computation. *Adv. Mater.* **2023**, *35*, 2303699.

(17) Zhang, J.; Guo, P.; Guo, Z.; Li, L.; Sun, T.; Liu, D.; Tian, L.; Zu, G.; Xiong, L.; Zhang, J.; Huang, J. Retina-inspired artificial synapses with ultraviolet to near-infrared broadband responses for energy-efficient neuromorphic visual systems. *Adv. Funct. Mater.* **2023**, *33*, 2302885.

(18) Zhu, Q.-B.; Li, B.; Yang, D.-D.; Liu, C.; Feng, S.; Chen, M.-L.; Sun, Y.; Tian, Y.-N.; Su, X.; Wang, X.-M.; Qiu, S.; Li, Q.-W.; Li, X.-M.; Zeng, H.-B.; Cheng, H.-M.; Sun, D.-M. A flexible ultrasensitive

optoelectronic sensor array for neuromorphic vision systems. *Nat. Commun.* **2021**, *12*, 1798.
(19) Huang, P.-Y.; Jiang, B.-Y.; Chen, H.-J.; Xu, J.-Y.; Wang, K.; Zhu, C.-Y.; Hu, X.-Y.; Li, D.; Zhen, L.; Zhou, F.-C.; Qin, J.-K.; Xu, C.-Y. Neuro-inspired optical sensor array for high-accuracy static image recognition and dynamic trace extraction. *Nat. Commun.* **2023**, *14*, 6736.
(20) Gu, L.; Li, X.; Xia, L.; Zhao, H.; Wang, B.; Li, Z.; Wang, Z. M.; Tong, X. Colloidal quantum dots-based photoelectrochemical-type optoelectronic synapse. *Adv. Funct. Mater.* **2024**, No. 2415178.
(21) Wang, Y.; Han, B.; Mayor, M.; Samorì, P. Opto-electrochemical synaptic memory in supramolecularly engineered Janus 2D MoS_2. *Adv. Mater.* **2024**, *36*, 2307359.
(22) Liu, Y.; Wu, Y.; Han, H.; Wang, Y.; Peng, R.; Liu, K.; Yi, D.; Nan, C. W.; Ma, J. $CuInP_2S_6$-based electronic/optoelectronic synapse for artificial visual system application. *Adv. Funct. Mater.* **2024**, *34*, 2306945.
(23) Feng, S.; Li, J.; Feng, L.; Liu, Z.; Wang, J.; Cui, C.; Zhou, O.; Deng, L.; Xu, H.; Leng, B.; Chen, X. Q.; Jiang, X.; Liu, B.; Zhang, X. Dual-mode conversion of photodetector and neuromorphic vision sensor via bias voltage regulation on a single device. *Adv. Mater.* **2023**, *35*, 2308090.
(24) Ma, H.; Fang, H.; Xie, X.; Liu, Y.; Tian, H.; Chai, Y. Optoelectronic synapses based on MXene/Violet phosphorus van der waals heterojunctions for visual-olfactory crossmodal perception. *Nano-Micro Lett.* **2024**, *16*, 104.
(25) Luo, J.; Tong, X.; Yue, S.; Wu, K.; Li, X.; Zhao, H.; Wang, B.; Li, Z.; Liu, X.; Wang, Z. M. Tailored environment-friendly reverse type-I colloidal quantum dots for a near-infrared optical synapse and artificial vision system. *ACS Nano* **2024**, *18*, 29991−30003.
(26) Gao, S.; Liu, G.; Yang, H.; Hu, C.; Chen, Q.; Gong, G.; Xue, W.; Yi, X.; Shang, J.; Li, R.-W. An oxide Schottky junction artificial optoelectronic synapse. *ACS Nano* **2019**, *13*, 2634−2642.
(27) Kumar, M.; Abbas, S.; Kim, J. All-oxide-based highly transparent photonic synapse for neuromorphic computing. *ACS Appl. Mater. Interfaces* **2018**, *10*, 34370−34376.
(28) Sun, Y.; Qian, L.; Xie, D.; Lin, Y.; Sun, M.; Li, W.; Ding, L.; Ren, T.; Palacios, T. Photoelectric synaptic plasticity realized by 2D perovskite. *Adv. Funct. Mater.* **2019**, *29*, 1902538.
(29) Wang, Y.; Lv, Z.; Chen, J.; Wang, Z.; Zhou, Y.; Zhou, L.; Chen, X.; Han, S. T. Photonic synapses based on inorganic perovskite quantum dots for neuromorphic computing. *Adv. Mater.* **2018**, *30*, 1802883.
(30) Wang, S.; Chen, C.; Yu, Z.; He, Y.; Chen, X.; Wan, Q.; Shi, Y.; Zhang, D. W.; Zhou, H.; Wang, X.; Zhou, P. A MoS_2/PTCDA hybrid heterojunction synapse with efficient photoelectric dual modulation and versatility. *Adv. Mater.* **2019**, *31*, 1806227.
(31) Luo, Z.-D.; Xia, X.; Yang, M.-M.; Wilson, N. R.; Gruverman, A.; Alexe, M. Artificial optoelectronic synapses based on ferroelectric field-effect enabled 2d transition metal dichalcogenide memristive transistors. *ACS Nano* **2020**, *14*, 746−754.
(32) Wang, Y.; Wang, K.; Hu, X.; Wang, Y. k.; Gao, W.; Zhang, Y.; Liu, Z.; Zheng, Y.; Xu, K.; Yang, D.; Pi, X. Optogenetics-inspired fluorescent synaptic devices with nonvolatility. *ACS Nano* **2023**, *17*, 3696−3704.
(33) Wang, Y.; Zhu, Y.; Li, Y.; Zhang, Y.; Yang, D.; Pi, X. Dual-modal optoelectronic synaptic devices with versatile synaptic plasticity. *Adv. Funct. Mater.* **2022**, *32*, 2107973.
(34) Yin, L.; Huang, W.; Xiao, R.; Peng, W.; Zhu, Y.; Zhang, Y.; Pi, X.; Yang, D. Optically stimulated synaptic devices based on the hybrid structure of silicon nanomembrane and perovskite. *Nano Lett.* **2020**, *20*, 3378−3387.
(35) Wu, X.; Zhang, Z.; Zhao, H.; Wang, Y.; Zhou, J.; Meng, D.; He, Y.; Liu, M.; Zhang, Y.; Xue, Z.; Jiang, C.; Zhang, M.; Di, Z.; Mei, Y.; Guo, Q. A skin-inspired optoelectromechanically coupled system for 3-axis airflow sensor. *Nano Energy* **2025**, *135*, 110659.
(36) Zhu, J.; Liu, C.; Gao, R.; Zhang, Y.; Zhang, H.; Cheng, S.; Liu, D.; Wang, J.; Liu, Q.; Wang, Z.; Wang, X.; Jin, Y.; Zhang, M. Ultra-flexible high-linearity silicon nanomembrane synaptic transistor array. *Adv. Mater.* **2025**, *37*, 2413404.
(37) Chen, Y.; Wei, Q.; Yin, J.; Xia, Y.; Liu, Z. Silicon-based hybrid optoelectronic devices with synaptic plasticity and stateful photoresponse. *Adv. Electron. Mater.* **2018**, *4*, 1800242.
(38) Pan, R.; Guo, Q.; Li, G.; Song, E.; Huang, G.; An, Z.; Di, Z.; Mei, Y. Schottky barrier modulation in surface nanoroughened silicon nanomembranes for high-performance optoelectronics. *ACS Appl. Mater. Interfaces* **2018**, *10*, 41497−41503.
(39) Feng, P.; Monch, I.; Harazim, S.; Huang, G.; Mei, Y.; Schmidt, O. G. Giant persistent photoconductivity in rough silicon nanomembranes. *Nano Lett.* **2009**, *9*, 3453−3459.
(40) Wang, Y.; Yin, L.; Huang, S.; Xiao, R.; Zhang, Y.; Li, D.; Pi, X.; Yang, D. Silicon-nanomembrane-based broadband synaptic phototransistors for neuromorphic vision. *Nano Lett.* **2023**, *23*, 8460−8467.
(41) Kim, M.-K.; Lee, J.-S. Short-term plasticity and long-term potentiation in artificial biosynapses with diffusive dynamics. *ACS Nano* **2018**, *12*, 1680−1687.
(42) Zhang, Z.; Li, T.; Wu, Y.; Jia, Y.; Tan, C.; Xu, X.; Wang, G.; Lv, J.; Zhang, W.; He, Y.; Pei, J.; Ma, C.; Li, G.; Xu, H.; Shi, L.; Peng, H.; Li, H. Truly concomitant and independently expressed short-and long-term plasticity in a Bi_2O_2Se-based three-terminal memristor. *Adv. Mater.* **2019**, *31*, 1805769.
(43) Han, C.; Han, J.; He, M.; Han, X.; Wu, Z.; Yu, H.; Gou, J.; Wang, J. Photonic synaptic transistor with memory mode switching for neuromorphic visual system. *Laser Photonics Rev.* **2024**, *18*, 2300976.
(44) Matsuzawa, T.; Aoki, Y.; Takeuchi, N.; Murayama, Y. A new long phosphorescent phosphor with high brightness, $SrAl_2O_4$:Eu^{2+},Dy^{3+}. *J. Electrochem. Soc.* **1996**, *143*, 2670.
(45) Green, M. A.; Keevers, M. J. Optical properties of intrinsic silicon at 300 K. *Prog. Photovolt: Res. Appl.* **1995**, *3*, 189−192.
(46) Sim, K.; Chen, S.; Li, Z.; Rao, Z.; Liu, J.; Lu, Y.; Jang, S.; Ershad, F.; Chen, J.; Xiao, J.; Yu, C. Three-dimensional curvy electronics created using conformal additive stamp printing. *Nat. Electron.* **2019**, *2*, 471−479.
(47) Hu, Y.; Zhuang, W.; Ye, H.; Zhang, S.; Fang, Y.; Huang, X. Preparation and luminescent properties of (Ca1-x, Srx)S:Eu2+ red-emitting phosphor for white LED. *J. Lumin.* **2005**, *111*, 139−145.

https://doi.org/10.1021/acs.nanolett.5c02135
Nano Lett. 2025, 25, 11836−11843